

CR2PQ: CONTINUOUS RELATIVE ROTARY POSITIONAL QUERY FOR DENSE VISUAL REPRESENTATION LEARNING

Anonymous authors

Paper under double-blind review

ABSTRACT

Dense visual contrastive learning (DRL) shows promise for learning localized information in dense prediction tasks, but struggles with establishing pixel/patch correspondence across different views (cross-contrasting). Existing methods primarily rely on self-contrasting the same view with variations, limiting input variance and hindering downstream performance. This paper delves into the mechanisms of self-contrasting and cross-contrasting, identifying the crux of the issue: transforming discrete positional embeddings to continuous representations. To address the correspondence problem, we propose a Continuous Relative Rotary Positional Query (CR2PQ), enabling patch-level representation learning. Our extensive experiments on standard datasets demonstrate state-of-the-art (SOTA) results. Compared to the previous SOTA method (PQCL), our approach achieves significant improvements on COCO: with 300 epochs of pretraining, CR2PQ obtains **3.4%** mAP^{bb} and **2.1%** mAP^{mk} improvements for detection and segmentation tasks, respectively. Furthermore, CR2PQ exhibits faster convergence, achieving **10.4%** mAP^{bb} and **7.9%** mAP^{mk} improvements over SOTA with just 40 epochs of pretraining.

1 INTRODUCTION

Self-supervised representation learning (SSL) has been attracting increasing attention in deep learning, whereby the prediction problem is often formulated as a pretext task with pre-training on unlabeled data. SSL methods can mainly be divided into three categories: **1) generative-based** methods (Donahue & Simonyan, 2019; Goodfellow et al., 2014), learning to generate samples in the input space; However, generation can be computationally expensive and may not be necessary for representation learning. **2) contextual-based** methods (Gidaris et al., 2018), designing pretext tasks (*e.g.*, denoising auto-encoders (Vincent et al., 2008), context autoencoders (Zhang et al., 2016), etc) to pretrain the backbone; **3) contrastive-based** methods (Chen et al., 2020a;b; 2021; He et al., 2020), taking augmented views of the same image as positive pairs and others as negative pairs. Contrastive-based methods have shown great promise in downstream tasks, *e.g.*, image classification/detection (Cai & Vasconcelos, 2018; He et al., 2017) and video classification (Han et al., 2020).

Contrastive learning is a family of instance discrimination-based methods (Chen et al., 2020a;b; 2021; He et al., 2020), which trains the network by distinguishing positive image-level samples from their negative counterparts given query anchors from mini-batches during the learning process. These general (instance-level) contrastive learning (Oord et al., 2018; Tian et al., 2020a) and its many variants (Caron et al., 2021; Song & Ermon, 2020; Zhou et al., 2022) are one of the most popular directions that achieved great success in the past few years and dominate other methods (generative-based and contextual-based) in the field of SSL, especially for linear and finetuning classification tasks.

However, these methods (Caron et al., 2021; Chen et al., 2020a; Grill et al., 2020) are still less competitive on dense predictive tasks (Wang et al., 2021; Xie et al., 2021c), *e.g.*, detection (He et al., 2017) and segmentation (Xiao et al., 2018). The main reason is that instance-level contrastive methods aim to learn global-discriminative information, but lack spatial-sensitive information. To address this issue, some dense contrastive learning (DCL) methods with pixel-wise (Wang et al., 2021; Xie et al., 2021c) and patch-wise (Yun et al., 2022) contrastive objectives and frameworks are proposed. However, these methods still have other limitations: **One main shortcoming** of these

dense contrastive learning methods is establishing the correspondence among pixels/patches usually requires bilinear interpolation, which is complex and heavily sensitive to random crop augmentation (in an extreme case, if two views have no intersection parts, there are no correspondence relation). One simple way to avoid mining the correspondence is inputting the same view (masked and unmasked versions) twice (Zhou et al., 2022). However, the variance of the inputs (masked and unmasked views) is much lower than inputting two different views, where the variance of two views has been proven to be the key to success in contrastive learning (Tian et al., 2020b; Wang et al., 2022a).

To address the correspondence problem, we propose a continuous rotary positional-query-based paradigm. Specifically, we first randomly crop two views from the image, and use the [relative coordinate system](#) and rotary positional embedding to represent the relative positions between the two views. Then, we take the rotary relative positional embedding as a query and reconstruct the latent representations (or RGB value) of one view from the other view. Through the [relative coordinate system](#) rotary positional query, our CR2PQ significantly simplifies the previous DCL paradigm (usually using GCN or other sub-network to learn the correspondence information), making the dense contrastive learning correspondence-free. Our main contributions are:

i) Correspondence-free DCL via relative coordinate system and continuous rotary positional embedding. Instead of simply employing RoPE to the vision domain (1D to 2D), we further transform the discrete positional embedding to continuous, taking the relative coordinates as input, which makes our CR2PQ correspondence-free. Besides, due to the simplicity of CR2PQ, our methods can be integrated into several popular representation learning paradigms, *e.g.*, MIM-based, CL-based, and Distillation-based methods (See Table 4).

ii) Positional-aware query module. Instead of directly using the vanilla self attention (Vaswani et al., 2017) (which would hurt the downstream performance and bring more computational cost due to the extra query tokens, as the downstream task only [inputs](#) the raw tokens), we propose positional-aware cross attention module in the final block between query tokens and patches embeddings to learn semantic information of query tokens, and the cross attention mechanism only incurs a few extra parameters.

iii) New SOTA performance. We conduct [exhaustive](#) experiments on classification, detection, and segmentation tasks, where our CR2PQ achieves new SOTA results. In particular, CR2PQ outperforms previous DCL methods with a large range, especially on dense prediction tasks. Specifically, it outperforms previous SOTA by **3.4%**, and **2.1%** points for detection and segmentation on the MSCOCO dataset. CR2PQ surpasses previous SOTA PQCL **1.9%** points on ADE20K semantic segmentation. We further conduct experiments to show its convergence speed, and we surprisingly find with few epochs (*e.g.*, 40) pretraining, CR2PQ outperforms previous SOTA DCL methods (Zhang et al., 2023a) **10.4%** and **7.9%** scores on detection and segmentation on the MSCOCO dataset.

2 RELATED WORKS

Instance contrastive learning. Instance self-supervised learning aims to extract informative image representations by leveraging unlabeled data. It achieves this by applying contrastive objectives, which essentially bring similar representations closer while pushing dissimilar ones further apart. A key challenge in contrastive learning is handling negative examples, which are data points used to differentiate the representation of the target image. Memory-based methods like MoCo (Chen et al., 2020b; He et al., 2020) store negative examples in a memory bank for comparisons. SimCLR (Chen et al., 2020a), on the other hand, treats all other data points within the same batch as negative examples. To avoid the need for explicit negative examples, BYOL (Grill et al., 2020) and SimSiam (Chen & He, 2021) employ separate encoder and predictor networks with a stop-gradient mechanism. Barlow Twins (Zbontar et al., 2021), ZeroCL (Zhang et al., 2021), and VICReg (Bardes et al., 2022) achieve similar results by focusing on decorrelating features at different levels. Building upon ZeroCL (Zhang et al., 2021), ARB (Zhang et al., 2022) proposes aligning representations with an orthogonal base for computational efficiency. Inspired by the success of Vision Transformers (ViTs), recent work like MoCo v3 (He et al., 2020) and DINO (Caron et al., 2021) are replacing convolutional neural networks (CNNs) with ViT backbones.

Dense contrastive self-supervised learning. In contrast to general contrastive learning, dense contrastive learning (Ge et al., 2021; Wang et al., 2021; Yang et al., 2021; Ziegler & Asano, 2022) methods aim to learn spatial-sensitive information to provide a pretrained model to dense predictive

tasks (*e.g.*, object detection, instance segmentation and semantic segmentation). DenseCL (Wang et al., 2021) exploits the correspondence by sorting the similarities of pixels in the deep feature map, while PixPro (Xie et al., 2021c) utilizes the augmentation wrapper to get the spatial correspondence of the pixel intersection between two views. Furthermore, Detco (Xie et al., 2021a) tries to improve the performance of general contrastive learning approaches by augmenting multiple global and local views simultaneously. Inspired by PixPro, Resim (Xiao et al., 2021) uses RoI Pooling (Jiang et al., 2018) to extract a feature vector from the associated feature map region for both views. On the basis of DenseCL, SetSim (Wang et al., 2022b) employs a threshold selection to filter out noisy backgrounds. With the development of ViT in SSL (Dosovitskiy et al., 2020), SelfPatch (Yun et al., 2022) treats the spatial neighbors of the patch as positive examples for learning more semantically meaningful relations among patches. On the basis of DINO (Caron et al., 2021), ADCLR (Zhang et al., 2023b) proposes patch-level contrasting via unmasked query tokens and cross-attention mechanism to avoid mining spatial correspondence. To further increase the variance of patch-level contrasting, PQCL (Zhang et al., 2023a) proposes to replace the unmasked query tokens with the relative positional embeddings, which further increase the difficulty of DCL, resulting in better performance in dense predictive tasks.

Masked Image Modeling (MIM). Masked Image Modeling (MIM) is a self-supervised learning technique where the model reconstructs masked portions of an image to learn meaningful representations. MIM methods can be categorized based on the information they reconstruct: (a) raw pixel values, (b) auxiliary features, and (c) masked patch embeddings. SimMIM (Xie et al., 2022) and MAE (He et al., 2021) (a) reconstruct the raw pixel values from masked or partially observed patches. MaskFeat (Wei et al., 2021) (b) incorporates HOG features as supervisory signals for richer semantics. CIM (Fang et al., 2022) (a) enhances robustness by adding perturbations to raw images. iBOT (Zhou et al., 2022) (c) is the first to predict token embeddings, but using the same view might influence downstream tasks. SIM (Tao et al., 2022) (c) addresses this by predicting masked patch embeddings from a different view, but introduces higher computational cost. MIM research offers a promising approach for learning powerful image representations for various computer vision tasks.

RoPE in vision domain. Relative Positional Encoding (RoPE) (Su et al., 2024) has emerged as a promising technique to improve vision transformers. Pioneering studies introduced RoPE to ViT-based architectures, with the Hybrid X-former (Jeevan & Sethi, 2022) applying 1D RoPE. While this approach demonstrates the potential of RoPE, its limitations in capturing spatial relationships hinder performance on complex vision tasks like classification, detection, and segmentation. Additionally, evaluations using small datasets might not accurately reflect the effectiveness of RoPE on larger and more intricate datasets. Recent studies exploring 2D RoPE, such as EVA-02 (Fang et al., 2023) and Unified-IO 2 (Lu et al., 2023), focused on language-related tasks or new model architectures. This work aims to bridge this gap by investigating the effectiveness of 2D RoPE in improving the performance of basic architectures on challenging vision tasks.

3 METHODOLOGY

3.1 PRELIMINARIES

APE and Vision Transformers. Denote an image by $\mathbf{x} \in \mathbb{R}^{C \times H \times W}$, where $H \times W$ is the resolution of the image and C is the number of channels. Plain ViT (Dosovitskiy et al., 2020) treats the image \mathbf{x} as a sequence composed of non-overlapping patches $\{\mathbf{x}^{(i)} \in \mathbb{R}^{CP^2}\}_{i=1}^N$, where each patch has a fixed $P \times P$ resolution. Then, the patches are linearly transformed to D -dimensional patch embeddings $\mathbf{z}^{(i)} = \mathbf{E}\mathbf{x}^{(i)} + \mathbf{P}_{pos}^i \in \mathbb{R}^D$, where $\mathbf{E} \in \mathbb{R}^{D \times CP^2}$ is the linear projection and $\mathbf{P}_{pos}^i \in \mathbb{R}^D$ is the positional embedding for the i -th patch. A $[CLS]$ token $\mathbf{z}^{([CLS])} \in \mathbb{R}^D$ is subsequently prepended to the patch sequence to extract global information, so the resulting input sequence is represented as $\mathbf{z} = [\mathbf{z}^{([CLS])}, \mathbf{z}^{(1)}, \mathbf{z}^{(2)}, \dots, \mathbf{z}^{(N)}]$. Then, ViT uses a Transformer encoder (Vaswani et al., 2017) to generate both image-level ($[CLS]$ token) and patch-level (other tokens). In line with SelfPatch (Yun et al., 2022), we use f_θ to denote the whole process of a ViT parameterized by θ :

$$f_\theta(\mathbf{x}) = f_\theta \left([\mathbf{z}^{([CLS])}, \mathbf{z}^{(1)}, \mathbf{z}^{(2)}, \dots, \mathbf{z}^{(N)}] \right) = [\mathbf{o}^{([CLS])}, \mathbf{o}^{(1)}, \mathbf{o}^{(2)}, \dots, \mathbf{o}^{(N)}] \quad (1)$$

where $\mathbf{o}^{([CLS])}$ and $\mathbf{o}^{(i)}$ are the representations of the whole image and i -th patch, respectively.

Rotary positional embedding in 1-D. In Transformer models, self-attention plays a crucial role in capturing relationships between words in a sentence. However, self-attention mechanisms lack

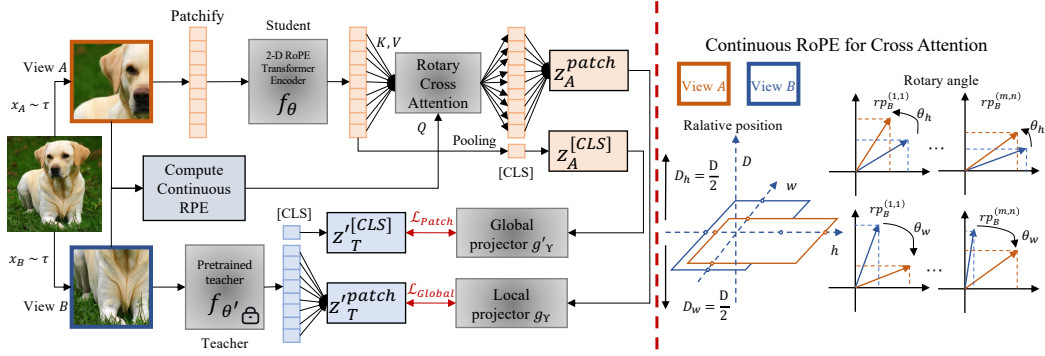


Figure 1: framework of the proposed CR2PQ. We first crop the image twice along with augmentations to generate view A and view B . Then, we compute the continuous relative position of the two views (illustrated in the right figure). For view A and view B , we feed them into the transformer encoder and the pre-trained teacher network, respectively. Then, we use the pre-calculated rotary positional embedding to extract patch-level embeddings of view B through the rotary cross-attention block. Finally, the patch-level and global alignment objectives are added to learn dense representations.

inherent knowledge of word order. Positional encoding techniques address this by injecting positional information into the model. Traditional relative positional encoding (RPE) methods, like relative positional bias (RPB), are often limited by the interaction with attention weights, which causes limited utilization of relative position. Thus, RoFormer (Su et al., 2024) proposes a novel relative position embedding method: Rotary Position Embedding (RoPE). RoPE directly incorporates relative position information into the attention computation by applying trigonometric functions (sine and cosine) to key and query vectors. This allows RoPE to interact effectively with attention weights, leading to a comprehensive understanding of word order within the self-attention process. Specifically, RoPE introduces the multiplication of Euler’s formula ($e^{i\theta}$) to key and query vectors as relative position embedding, *i.e.*, when n, m -th query and keys in $\mathbf{q}_n, \mathbf{k}_m \in \mathbb{R}^{1 \times D_{head}}$, RoPE is applied as follows:

$$\mathbf{q}'_n = \mathbf{q}_n e^{in\theta}, \quad \mathbf{k}'_m = \mathbf{k}_m e^{im\theta}, \quad \text{Attn}_{n,m} = \text{Re}[\mathbf{q}'_n \mathbf{k}'_m] = \text{Re}[\mathbf{q}_n \mathbf{k}_m^* e^{i(n-m)\theta}] \quad (2)$$

where $\text{Re}[\cdot]$ denotes real part of complex number and $*$ means complex conjugates.

3.2 THE PROPOSED CR2PQ

View Generation. Given the image $\mathbf{x} \in \mathbb{R}^{H \times W \times 3}$ in training set, we first randomly crop the image twice to generate two views \mathbf{x}_A and \mathbf{x}_B . Then, we resize the two views to $H \times W \times 3$. Note that we randomly crop two views, therefore, the positional relationship of the two views might be either containing, overlapping, or non-overlapping. We record the absolute position \mathbf{p}_A of \mathbf{x}_A and \mathbf{p}_B of \mathbf{x}_B , respectively. Specifically, \mathbf{p}_A and \mathbf{p}_B are composed of $\mathbf{p}_A = \{p_{Ai}, p_{Aj}, p_{Ah}, p_{Aw}\}$ (top location, left location, height and width) and $\mathbf{p}_B = \{p_{Bi}, p_{Bj}, p_{Bh}, p_{Bw}\}$, respectively.

Computing Relative Positional Coordinates. The core idea of our CR2PQ is to use the [relative coordinate system](#) and continuous rotary positional embeddings to represent the positional relationship between the two views. For simplicity, we use view A to reconstruct view B as an example. Specifically, Suppose the grid size of the feature map of the view A is K_A . Then, the patch index matrix of view A can be written as:

$$\mathbf{rp}_A = \begin{pmatrix} (0, 0) & (0, 1) & (0, 2) & \cdots & (0, K_A^W - 1) \\ (1, 0) & (1, 1) & (1, 2) & \cdots & (1, K_A^W - 1) \\ (2, 0) & (2, 1) & (2, 2) & \cdots & (2, K_A^W - 1) \\ \vdots & \vdots & \vdots & \vdots & \vdots \\ (K_A^H - 1, 0) & (K_A^H - 1, 1) & (K_A^H - 1, 2) & \cdots & (K_A^H - 1, K_A^W - 1) \end{pmatrix} \quad (3)$$

where $K_A^H = H/ps_A$, and $K_A^W = W/ps_A$, and ps_A is the patch size when inputting the view A to the model. Observed through Eq. 3, we can recognize the patch index matrix \mathbf{rp}_A as a 2-D coordinates system, where the top-left element is the origin point and the scale of the coordinates system is 1. The detailed illustration can be found in Fig. 2. Since we set each grid size of the feature map of the anchor view as 1, then the relative positional indices (relative coordinates) of the patches

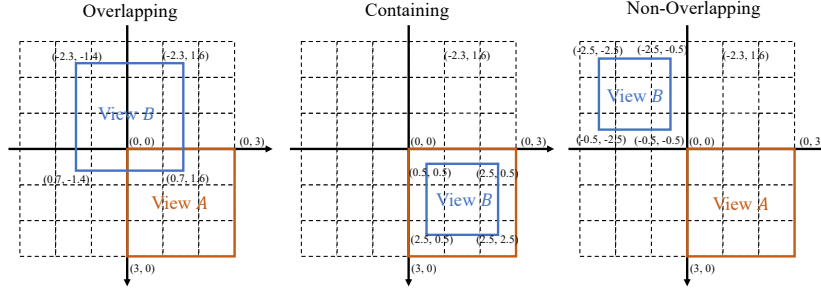


Figure 2: Illustration of three different scenarios (overlapping, containing, and non-overlapping). The proposed relative coordinate system can easily represent the relative coordinate matrix \mathbf{rp}_B in both three scenarios. We always use the top-left corner of the view A as the origin point and set the interval of the feature map of view A as 1.

of the view B can be written as:

$$\mathbf{rp}_B^{m,n}(ps_A, ps_B) = \left(\underbrace{\frac{K_A^H \cdot (p_{Bi} - p_{Ai})}{p_{Ah}} + \frac{p_{bh} \cdot K_A^H \cdot (m-1)}{K_B^H \cdot p_{Ah}}}_{\text{Row}}, \underbrace{\frac{K_A^W \cdot (p_{Bj} - p_{Aj})}{p_{Aw}} + \frac{p_{Bw} \cdot K_A^W \cdot (n-1)}{K_B^W \cdot p_{Aw}}}_{\text{Column}} \right) \quad (4)$$

where $(\mathbf{rp}_B^m, \mathbf{rp}_B^n)$ is the m -th row n -th column element in the coordinate matrix \mathbf{rp}_B . ps_B is the patch size when inputting the view B to the model, and $K_B^H = H/ps_B$, $K_B^W = W/ps_B$. Note that ps_A and ps_B are dependent on the patch size of the predefined backbone and teacher networks.

Continuous Relative Rotary Positional Embeddings. Given the coordinate indices matrix \mathbf{rp}_A of view A , suppose the hidden dimensions of each head of the backbone is D_{head} , then we first convert query and key to $\mathbb{C}^{1 \times (D_{head}/4)}$ by considering the $2t$ -th dim as real part and $2t+1$ -th dim as imaginary part. For each channel, following RoPE (Su et al., 2024), we utilize multiple frequencies θ_t in the key and query, i.e., $\theta_t = 10000^{-t/(D_{head}/2)}$, where $t \in \{0, 1, \dots, D_{head}/4\}$. Then, for the m -th row and n -th column location in the positional matrix in Eq. 3 of view A , the rotation matrix $\mathbf{R}_{rot} \in \mathbb{C}^{(K_A^H K_A^W) \times D_{head}/4}$ can be written as:

$$\begin{aligned} \mathbf{R}_{rot}^{(m,n,2t)} &= e^{i\theta_t m}, \quad \mathbf{R}_{rot}^{(m,n,2t+1)} = e^{i\theta_t m}, \quad 0 \leq t < D_{head}/2 \\ \mathbf{R}_{rot}^{(m,n,2t)} &= e^{i\theta_t n}, \quad \mathbf{R}_{rot}^{(m,n,2t+1)} = e^{i\theta_t n}, \quad D_{head}/2 \leq t < D_{head} \end{aligned} \quad (5)$$

Then, for view B , we can replace the m, n in Eq. 5 with $\frac{K_A^H \cdot (p_{Bi} - p_{Ai})}{p_{Ah}} + \frac{p_{bh} \cdot K_A^H \cdot (m-1)}{K_B^H \cdot p_{Ah}}$ and $\frac{K_A^W \cdot (p_{Bj} - p_{Aj})}{p_{Aw}} + \frac{p_{Bw} \cdot K_A^W \cdot (n-1)}{K_B^W \cdot p_{Aw}}$, respectively. Then, the relative rotary matrix becomes to:

$$\mathbf{R}_{rela}^{(m,n)} = \begin{cases} e^{i\theta_t \left[\frac{K_A^H \cdot (p_{Bi} - p_{Ai})}{p_{Ah}} + \frac{p_{bh} \cdot K_A^H \cdot (m-1)}{K_B^H \cdot p_{Ah}} \right]}, & 0 \leq t < D_{head}/2 \\ e^{i\theta_t \left[\frac{K_A^W \cdot (p_{Bj} - p_{Aj})}{p_{Aw}} + \frac{p_{Bw} \cdot K_A^W \cdot (n-1)}{K_B^W \cdot p_{Aw}} \right]}, & D_{head}/2 \leq t < D_{head} \end{cases} \quad (6)$$

where $2t$ -th dims are the real part and $2t+1$ -th dims are the imaginary part.

Framework and Objectives. Given the cropped views $\mathbf{x}_A, \mathbf{x}_B$, we first calculate the relative positions \mathbf{rp}_A and \mathbf{rp}_B . Then, we calculate the rotary matrix \mathbf{R}_{rot} and relative rotary \mathbf{R}_{rela} via Eq. 5 and Eq. 6, respectively. Then, we feed the \mathbf{x}_A to the encoder network, which is composed of a patchify layer and several transformer blocks. For each block, we replace the self-attention with:

$$\text{Attn}(\mathbf{Q}, \mathbf{K}, \mathbf{V})^{(m,n)} = \sum_{h=0}^{K_A^{H-1}} \sum_{w=0}^{K_A^{W-1}} \frac{\exp \left((\mathbf{R}_{rot}^{(m,n)} \mathbf{q}^{(m,n)})^\top (\mathbf{R}_{rot}^{(h,w)} \mathbf{k}^{(h,w)}) \right)}{\sum_{h=0}^{K_A^{H-1}} \sum_{w=0}^{K_A^{W-1}} \exp \left((\mathbf{R}_{rot}^{(m,n)} \mathbf{q}^{(m,n)})^\top (\mathbf{R}_{rot}^{(h,w)} \mathbf{k}^{(h,w)}) \right)} \mathbf{v}^{(h,w)} \quad (7)$$

where $\mathbf{q}^{(m,n)} = \mathbf{h}^{(m,n)} \mathbf{W}_Q$, $\mathbf{k}^{(m,n)} = \mathbf{h}^{(m,n)} \mathbf{W}_K$, and $\mathbf{v}^{(m,n)} = \mathbf{h}^{(m,n)} \mathbf{W}_V$, where $\mathbf{h}^{(m,n)}$ is the hidden representation of the patch located in m -th row and n -th column. $\mathbf{W}_Q, \mathbf{W}_K, \mathbf{W}_V$ are

learnable parameters. Given the parameterized backbone by f_θ , we can calculate the representation of the view A by $\mathbf{h}_A = f_\theta(\mathbf{x}_A, \mathbf{R}_{rot})$. Then, the position-aware cross attention becomes:

$$\mathbf{h}^{\mathbf{r}p_B^{m,n}} = \sum_{h=0}^{K_A^H-1} \sum_{w=0}^{K_A^W-1} \frac{\exp\left(\left(\mathbf{R}_{rela}^{(m,n)} \Phi(\mathbf{r}p_B^{(m,n)})\right)^\top (\mathbf{R}_{rot}^{(h,w)} \mathbf{k}^{(h,w)})\right) \mathbf{v}^{(h,w)}}{\sum_{h=0}^{K_A^H-1} \sum_{w=0}^{K_A^W-1} \exp\left(\left(\mathbf{R}_{rela}^{(m,n)} \Phi(\mathbf{r}p_B^{(m,n)})\right)^\top (\mathbf{R}_{rot}^{(h,w)} \mathbf{k}^{(h,w)})\right)} \quad (8)$$

where $\mathbf{R}_{rela}^{(m,n)}$ is given by Eq. 6, and $\mathbf{r}p_B^{(m,n)}$ is the m -th row n -th column elements of the relative coordinate matrix $\mathbf{r}p_B$, as derived by Eq. 4. $\Phi(\mathbf{r}p_B^{(m,n)}) = (\mathbf{q}^{(m,n)} + \mathbf{h}_{mask})\mathbf{W}_Q$, where \mathbf{h}_{mask} is the learnable masked placeholder, which is also commonly used in other methods (Xie et al., 2022; Zhou et al., 2022), and \mathbf{W}_Q is the learnable parameters. After obtaining the $\mathbf{h}^{\mathbf{r}p_B}$, we feed the $\mathbf{h}^{\mathbf{r}p_B}$ to the light-weight decoder g_γ to obtain \mathbf{z}_B , and predict the embedding or RGB pixel values of the view B . Specifically, for distillation methods, we adopt a pretrained encoder $f'_\theta(\cdot)$, and extract the hidden representations by $\mathbf{z}'_B = f'_\theta(\mathbf{x}_B)$, where $\mathbf{z} \in \mathbb{R}^{K_B^H \times K_B^W \times D_{tea}}$, where D_{tea} is the output dimension of the teacher model. Finally, we compute the patch-level objective by:

$$\mathcal{L}_{Patch} = \frac{1}{K_B^H K_B^W} \sum_{h=1}^{K_B^H} \sum_{w=1}^{K_B^W} \left\| \mathbf{z}_B^{(h,w)} - \mathbf{z}'_B^{(h,w)} \right\|_p^p, \quad (9)$$

Meanwhile, we add another global objective term to learn global-discriminative information by:

$$\mathcal{L}_{Global} = \left\| g'_\gamma \left(\frac{1}{K_B^H K_B^W} \sum_{h=1}^{K_B^H} \sum_{w=1}^{K_B^W} \mathbf{h}_T^{(h,w)} \right) - \frac{1}{K_B^H K_B^W} \sum_{h=1}^{K_B^H} \sum_{w=1}^{K_B^W} \mathbf{z}'_T^{(h,w)} \right\|_p^p, \quad (10)$$

where g'_γ is the global projector composed of two linear layers and an activation function. Finally, we adopt a hyper-parameter to balance the global and local objectives $\mathcal{L}_{CR2PQ} = \mathcal{L}_{Patch} + \lambda \cdot \mathcal{L}_{Global}$.

4 EXPERIMENTS

Datasets. We conduct self-supervised pre-training on the ImageNet-1K (Deng et al., 2009) training set with 1,000 classes, as used in SSL for both MIM (He et al., 2021) and contrastive learning (Chen et al., 2020a). We also transfer the encoder pre-trained by CR2PQ on MS-COCO (Lin et al., 2014) and ADE20K (Zhou et al., 2017) datasets.

Pre-training hyper-parameters. In line with CAE (Chen et al., 2022), we train with Adamw (Loshchilov & Hutter, 2018) and a batch size of 2048, distributed over 32 GPUs using ViT-S/16 (batch size per GPU is 64). For ViT-B, the learning rate is linearly ramped up during the first 40 epochs to its base value determined with the following linear scaling rule (Chen et al., 2020a): $blr = 1.5e-4$, $BatchSize=2048$, and $lr = blr * BatchSize/256$. For ViT-S, we set blr as $1.75e-4$. After warmup, we decay the learning rate with a cosine schedule (Loshchilov & Hutter, 2016). We follow the data augmentations of BYOL (Grill et al., 2020) (color jittering, Gaussian blur, and solarization) with a bicubic interpolation to adapt the position embeddings to the scales.

Platform. The experiments are performed on a workstation with 32 V100 GPUs by default (if not otherwise specified).

4.1 MAIN RESULTS

COCO object detection and segmentation. Setups. We evaluate pre-trained models on the COCO object detection and instance segmentation tasks (Lin et al., 2014). We evaluate our model under two popular frameworks Mask-RCNN (He et al., 2017) and Cascade R-CNN (Cai & Vasconcelos, 2018) with the standard 1x schedule (12 epochs). In line with previous methods (Zhang et al., 2023a; Zhou et al., 2022), we adopt AdamW (Loshchilov & Hutter, 2018) optimizer and set the learning rate as $3e-4$ with weight decay 0.05. **Evaluation.** MS COCO (Lin et al., 2014) is a large-scale object detection, segmentation, and captioning dataset: in particular, train 2017 and val 2017 splits contain 118K and 5K images, respectively. We follow the basic configuration of mmdetection (Chen et al., 2019) for fine-tuning Mask R-CNN (He et al., 2017) with FPN (Lin et al., 2017) under the standard 1x schedule. **Results.** Table 1 shows the proposed CR2PQ can consistently outperform previous SOTA (Zhang et al., 2023a) in both object detection and instance segmentation tasks. We evaluate CR2PQ with both

Table 1: **Accuracy on MS-COCO.** Mask R-CNN (He et al., 2017) and Cascade R-CNN (Cai & Vasconcelos, 2018) are adopted and trained with the 1x schedule. All the results are obtained by using our same finetune protocol for fair comparisons. Epoch refers to the number of pretraining.

Method	Backbone	Framework	#Epochs	#Param.	#Views.	Object Detection			Instance Segmentation		
						AP ^{bb}	AP ^{bb} ₅₀	AP ^{bb} ₇₅	AP ^{mk}	AP ^{mk} ₅₀	AP ^{mk} ₇₅
Moco-V2 (Chen et al., 2020b)	ResNet-50	Mask RCNN	200	23M	2×224^2	38.9	59.2	42.4	35.5	56.2	37.8
SwAV (Caron et al., 2020)	ResNet-50		200	23M	2×224^2	38.5	60.4	41.4	35.4	57.0	37.7
DenseCL (Wang et al., 2021)	ResNet-50		200	23M	2×224^2	40.3	59.9	44.3	36.4	57.0	39.2
ReSim (Xiao et al., 2021)	ResNet-50		200	23M	2×224^2	40.3	60.6	44.2	36.4	57.5	38.9
DetCo (Xie et al., 2021a)	ResNet-50		200	23M	2×224^2	40.1	61.0	43.9	36.4	58.0	38.9
Moco V3 (Chen et al., 2021)	ViT-S/16		300	23M	2×224^2	39.8	62.6	43.1	37.1	59.6	39.2
MoBY (Xie et al., 2021b)	ViT-S/16		300	22M	2×224^2	41.1	63.7	44.8	37.3	60.3	39.8
DINO (Caron et al., 2021)	ViT-S/16		300	22M	2×224^2	40.8	63.4	44.2	37.3	59.9	39.5
SelfPatch (Yun et al., 2022)	ViT-S/16		200	22M	2×224^2	42.1	64.9	46.1	38.5	61.3	40.8
iBOT (Zhou et al., 2022)	ViT-S/16		200	22M	2×224^2	42.6	65.7	47.0	39.0	61.7	41.3
PQCL (Zhang et al., 2023a)	ViT-S/16		200	22M	2×224^2	43.1	66.0	47.4	39.3	62.2	41.6
PQCL (Zhang et al., 2023a)	ViT-S/16		300	22M	2×224^2	44.0	66.7	48.1	39.7	63.1	42.2
CR2PQ (Ours)	ViT-S/16		200	22M	2×224^2	45.0	67.4	49.0	39.9	63.4	42.7
CR2PQ (Ours)	ViT-S/16		300	22M	2×224^2	47.4	69.3	52.0	41.8	65.9	44.7
DINO (Caron et al., 2021)	ViT-S/16	Cascade RCNN	300	22M	2×224^2	45.2	64.9	47.8	38.9	61.2	41.7
SelfPatch (Yun et al., 2022)	ViT-S/16		300	22M	2×224^2	46.6	65.7	48.8	39.5	62.0	42.6
DINO (Caron et al., 2021)	ViT-S/16		800	22M	$2 \times 224^2 + 10 \times 96^2$	46.8	66.7	50.3	40.6	63.7	43.2
iBOT (Zhou et al., 2022)	ViT-S/16		300	22M	2×224^2	45.4	65.1	49.0	39.6	62.1	41.7
iBOT (Zhou et al., 2022)	ViT-S/16		800	22M	$2 \times 224^2 + 10 \times 96^2$	49.4	68.7	53.3	42.6	65.6	45.8
PQCL (Zhang et al., 2023a)	ViT-S/16		200	22M	2×224^2	46.2	65.5	49.8	39.9	62.3	42.6
PQCL (Zhang et al., 2023a)	ViT-S/16		300	22M	2×224^2	47.7	67.0	51.3	41.1	64.0	44.2
RoPE (Su et al., 2024) (Scratch)	ViT-S/16		0	22M	2×224^2	31.0	47.1	33.4	27.7	44.9	29.2
CR2PQ (Ours)	ViT-S/16	RoPE (Su et al., 2024) (Scratch)	100	22M	2×224^2	49.4	68.1	53.5	42.7	65.4	46.1
CR2PQ (Ours)	ViT-S/16		200	22M	2×224^2	50.3	69.2	54.4	43.2	66.5	46.5
CR2PQ (Ours)	ViT-S/16		300	22M	2×224^2	50.5	69.5	54.7	43.4	66.7	46.8
CR2PQ (Ours)	ViT-S/16		300	22M	2×224^2	50.5	69.5	54.7	43.4	66.7	46.8

200 and 300 epochs pretraining. When applying the pre-trained model to Cascaded-RCNN, for 200 epochs pretraining without local views (Caron et al., 2020) and query views (Zhang et al., 2023a), CR2PQ surpasses PQCL (Zhang et al., 2023a) with 100 epochs pretraining and one extra query view pretraining **1.7%** point mAP^{bb} and **1.6%** point mAP^{mk}, respectively. Besides, our CR2PQ with 300 epochs pretraining can outperform iBOT (800 epochs pretraining with 10 extra local views) by **1.1%** point mAP^{bb} and **0.8%** point mAP^{mk}. When adopting the Mask-RCNN framework, under 200 epochs pretraining, our model CR2PQ outperforms PQCL by **1.9%** point mAP^{bb} and **0.6%** point mAP^{mk}, respectively. With 300 epochs pretraining, compared with previous SOTA PQCL (Zhang et al., 2023a), our CR2PQ achieves **3.4%** mAP^{bb} and **2.1%** mAP^{mk} improvements on detection and segmentation tasks, respectively. We also evaluate the detection and segmentation performance without pretraining, *i.e.*, directly using 2D RoPE (Su et al., 2024), where the 2D RoPE obtains much worse results than CR2PQ.

ADE20K semantic segmentation. Setup. We evaluate semantic segmentation performances of pre-trained models on ADE20K (Zhou et al., 2017), which contains 150 fine-grained semantic categories and 25K training data. We finetune the pre-trained models on Semantic FPN (Lin et al., 2017) and UperNet (Xiao et al., 2018) with 40K and 160K iteration, respectively. Following the previous methods SelfPatch (Yun et al., 2022) and PQCL (Zhang et al., 2023a), we report three metrics: (a) mean intersection of union (mIoU) averaged over all semantic categories, (b) all pixel accuracy (aAcc), and (c) mean class accuracy (mAcc). **Evaluation.** ADE20K (Zhou et al., 2017) is a semantic segmentation benchmark containing 150 fine-grained semantic categories and 25K images. We follow all the configurations of mmsegmentation (Contributors, 2020) for fine-tuning Semantic FPN (Lin et al., 2017) with 40K iterations and an input resolution of 512×512. We also perform large-scale fine-tuning experiments using UperNet (Xiao et al., 2018) with 160K iterations and an input resolution of 512×512. **Results.** As shown in Table 2, CR2PQ can outperform previous all methods under the same setting. Besides, we further evaluate DINO (Caron et al., 2021) with 10 local views and 800 epochs pretraining (checkpoint is downloaded in their official repository), where CR2PQ gets **2.6%** point improvements with only 200 epochs pretraining and only two global views. We guess the big improvements are because CR2PQ is a patch-level distillation method, which makes our method much more sensitive to spatial information, resulting the higher performance in dense prediction tasks.

4.2 ABLATION STUDIES

Fine-tuning classification. Most of the previous dense contrastive learning methods (Xie et al., 2021c; Yun et al., 2022) show worse performance compared with global instance-level contrastive methods (Caron et al., 2021; Zhou et al., 2022), which is because the patch-level loss could inhibit

Table 2: **ADE20K semantic segmentation** performances of the recent self-supervised approaches pre-trained on ImageNet. The metrics mIoU, aAcc, and mAcc denote the mean intersection of union, all pixel accuracy, and mean class accuracy, respectively.

Method	Arch	Backbone	#Iter	#Epochs	#Params	#Views	mIoU	aAcc	mAcc
MoCo-v2 (Chen et al., 2020b)	FPN	ResNet50	40k	200	23M	2×224^2	35.8	77.6	45.1
SwAV (Caron et al., 2020)	FPN	ResNet50	40k	200	23M	2×224^2	35.4	77.5	44.9
DenseCL (Wang et al., 2021)	FPN	ResNet50	40k	200	23M	2×224^2	37.2	78.5	47.1
MocoV3 (Chen et al., 2021)	FPN	ViT-S/16	40k	300	23M	2×224^2	35.3	78.9	45.9
MoBY (Xie et al., 2021b)	FPN	ViT-S/16	40k	300	23M	2×224^2	39.5	79.9	50.5
DINO (Caron et al., 2021)	FPN	ViT-S/16	40k	300	23M	2×224^2	38.3	79.0	49.4
DINO (Caron et al., 2021)	UperNet	ViT-S/16	160k	300	23M	2×224^2	42.3	80.4	52.7
SelfPatch (Yun et al., 2022)	FPN	ViT-S/16	40k	200	23M	2×224^2	41.2	80.7	52.1
SelfPatch (Yun et al., 2022)	UperNet	ViT-S/16	160k	200	23M	2×224^2	43.2	81.5	53.9
DINO (Caron et al., 2021)	UperNet	ViT-S/16	160k	800	23M	$2 \times 224^2 + 10 \times 96^2$	44.4	81.7	55.5
iBOT (Zhou et al., 2022)	UperNet	ViT-S/16	160k	200	23M	2×224^2	44.1	81.4	55.3
ADCLR (Zhang et al., 2023b)	UperNet	ViT-S/16	160k	200	23M	2×224^2	44.3	81.9	55.1
PQCL (Zhang et al., 2023a)	UperNet	ViT-S/16	160k	200	23M	2×224^2	45.1	82.0	56.1
CR2PQ (Ours)	UperNet	ViT-S/16	160k	200	23M	2×224^2	47.0	83.1	57.4

Table 3: Finetune top-1 and top-5 classification accuracies on ImageNet-1K with ViT-S and ViT-B. ‘‘PT Eps’’ and ‘‘FT Eps’’ mean the number of epochs for pretraining and fine-tuning, respectively.

Method	Backbone	#Params	PT Eps	FT Eps	Top-1	Top-5	Backbone	#Params	PT Eps	FT Eps	Top-1	Top-5
DeiT (Touvron et al., 2021)	ViT-S	22M	300	200	79.9	~	ViT-B	86M	300	100	81.2	~
MAE (He et al., 2021)	ViT-S	22M	1600	200	80.6	~	ViT-B	86M	300	100	83.2	~
Moco V3 (He et al., 2021)	ViT-S	22M	1600	200	81.4	~	ViT-B	86M	800	100	83.2	~
DINO (He et al., 2021)	ViT-S	22M	1600	200	81.5	~	ViT-B	86M	800	100	82.8	~
iBOT (Zhou et al., 2022)	ViT-S	22M	800	200	81.8	~	ViT-B	86M	300	100	83.2	~
TinyMIM (Ozbulak et al., 2023)	ViT-S	22M	300	100	81.5	85.8	ViT-B	86M	300	100	83.4	96.3
CR2PQ (Ours)	ViT-S	22M	300	200	82.2	86.1	ViT-B	86M	300	100	83.7	96.5

the model from learning global-discriminative information. However, different from previous DCL methods, we find CR2PQ could achieve comparable results on fine-tuning classification with the instance-level SSL methods. We guess that’s because we add the global objective in Eq. 10, which helps CR2PQ learn global-discriminative information. Table 3 shows the fine-tuning accuracies with different backbones (ViT-S and ViT-B). With ViT-S, CR2PQ achieves 82.2 top-1 accuracy with only 300 epochs pretraining, which outperforms previous SOTA iBOT (Zhou et al., 2022) with 800 epochs pretraining by 0.4 point. With ViT-B, our methods achieve 83.7 top-1 accuracies with only 300 epochs pretraining, which outperforms under the same epochs pretraining.

Teacher models and architectures. To explore the effect of the teacher model, we test our CR2PQ with different teacher models. Specifically, we adopt ViT-S (Dosovitskiy et al., 2020) as the student model and use ViT-B and ResNets (He et al., 2016) as the teacher model. As the output dimensions of different teacher models could be variant (*e.g.*, $14 \times 14 \times 768$ for ViT-B/16, $7 \times 7 \times 2048$ for ResNets), we change the grid size K_B^H and K_B^W of the relative positional index. More concretely, for ResNet-50 and ResNet-101, we set the grid size of the positional embeddings to $224/7 = 32$. For ViT-B/16, we set the grid size of the positional embeddings to $224/14 = 16$. We mainly choose the teacher model pre-trained by some profound methods, including MAE (He et al., 2021), iBOT (Zhou et al., 2022), and DINO (Caron et al., 2021). We keep the batch size as 2048 and use ViT-S/16 as the student network to train CR2PQ with 300 epochs. Table 4 shows the results with different teacher models. We find using contrastive-based teacher model (Caron et al., 2021; Chen et al., 2020a), our CR2PQ could obtain more gains than using MIM-based (He et al., 2021; Zhou et al., 2022) teacher models. We guess that’s because contrastive-based methods usually learn global-discriminative information, but lose local information. When using these contrastive-based methods, our CR2PQ could enhance the ability to capture the local information. In contrast, MIM-based methods usually add the patch-level objective, and the pre-trained models are more spatial-sensitive but less global-discriminative. Therefore, when using MIM-based methods as the teacher model, our CR2PQ may lose some global-discriminative information, leading to fewer improvements than using contrastive-based teacher models.

Table 4: Comparisons with different teachers.

Student	Teacher	Epoch	mAP ^{bb}	mAP ^{pmk}
ViT-B	EMA update (Contrastive)	300	44.1	39.8
	Pixel (Masked Image Modeling)		45.2	40.8 (+1.0)
	DINO (Caron et al., 2021) (Res-50)		47.4	41.8 (+2.0)
	DINO (Caron et al., 2021) (ViT-B)		47.0	41.1 (+1.3)
	SimCLR (Chen et al., 2020a) (Res-50)		47.1	41.6 (+1.8)
	MAE (He et al., 2021) (ViT-B)		46.5	40.7 (+0.9)
	MAE (He et al., 2021) (ViT-L)		47.0	41.4 (+1.6)
	iBOT (Zhou et al., 2022) (ViT-B)		46.2	41.0 (+1.2)
	iBOT (Zhou et al., 2022) (ViT-L)		46.8	41.5 (+1.7)

Loss weight of global semantic learning. As CR2PQ mainly focuses on dense prediction tasks, we set the weight of the global objective $\lambda = 0.5$ as the default. To better balance the global-

Table 5: **Ablation on projector head.** We pre-train all the models with 400 epochs and 2048 batch size on ImageNet-1K. We compare different architectures of heads. “Share weights” means the global and local projectors share the same weights. “Trans” means multi-head self-attention decoder.

Architecture	Share weights	Global projector	Local projector	Top-1	Top-5	Framework	mAP ^{bb}	mAP ^{mk}
ViT-B/16	✓	2-layer MLP	2-layer MLP	83.3	96.2	Cascade-RCNN	52.0	45.1
	✓	3-layer MLP	3-layer MLP	83.2	96.1		52.4	45.3
	✗	2-layer MLP	2-layer MLP	83.4	96.2		52.0	45.1
	✗	3-layer MLP	2-layer MLP	83.2	96.1		52.1	45.0
	✗	2-layer MLP	3-layer MLP	83.5	96.4		52.5	45.1
	✗	2-layer MLP	2-layer Trans	83.7	96.5		53.0	45.6

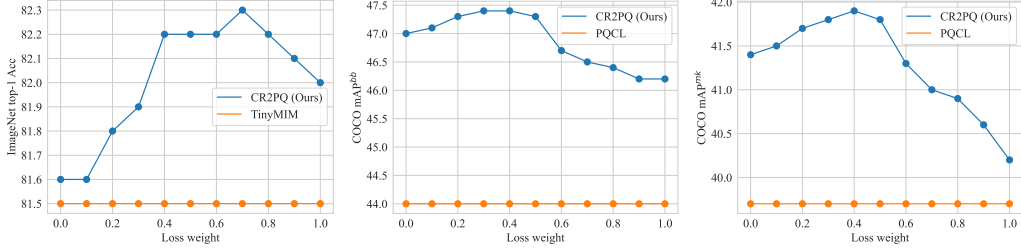


Figure 3: Finetuning classification on ImageNet-1K (left), object detection (middle) and instance segmentation (right) performance on COCO with different global and local objective weights λ . All the experimental settings keep the same for fair comparisons.

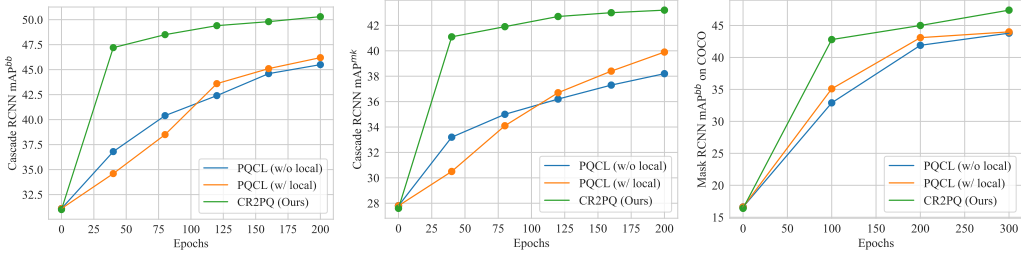


Figure 4: Finetuning Cascade-RCNN and Mask-RCNN (right) on detection (left) and segmentation (middle) on COCO dataset. We report the mAP^{bb} and mAP^{mk} performance for each 40 epochs.

discriminative and spatial-sensitive information, we further conduct a set of experiments by switching λ from 0 \sim 1. Specifically, we pre-train ViT-S/16 300 epochs with 2048 batch size. Then, for detection and segmentation, we finetune the pretrained model on COCO dataset with Mask RCNN framework. Fig. 3 illustrate the finetuning classification accuracy on ImageNet, mAP^{bb} and mAP^{mk} results on COCO with different global loss weight λ . We find with larger λ , CR2PQ obtains higher fine-tune accuracy on ImageNet-1K. However, correspondingly, large λ makes CR2PQ learn less spatial information, resulting mAP score drops on the COCO dataset. We also find when setting $\lambda = 0$, the detection score is also lower than $\lambda = 0.5$, we guess that’s because too small λ makes CR2PQ fail to learn global-discriminative information, where detection tasks also require the discriminative information to help classify the object in classification head layer.

Projector head of global semantic learning. To further study the effect of the local and global projector head, we try different combinations of the two modules. Following SimSiam (Chen & He, 2021) and Barlow Twins (Zbontar et al., 2021), we mainly attempt to use 2-layer and 3-layer MLP and 2-layer transformer blocks as projector heads. Since the global projector inputs one global token, we only add the transformer block on the local projector module. Table 5 shows fine-tuned classification, detection and instance segmentation results on ImageNet-1K and COCO datasets with different architectures. Different from previous contrastive methods (Chen & He, 2021; Zbontar et al., 2021), we find that lightweight global projectors can bring better classification accuracy than complex architectures, while employing two-layer transformer layer as local projector can bring more gains than simply using two-layer and three-layer MLP.

Pretraining Strategy. To show the effectiveness of our continuous rotary positional embedding, we conduct a set of experiments, including three types of positional embeddings, *i.e.*, continuous sin-cos

embedding, discrete rotary positional embedding (RoPE), learnable relative positional embeddings and discrete sin-cos embeddings. More concretely, for sin-cos embedding, we first calculate the relative positional index proposed in Eq. 4. Then, for each index, we calculate the sin-cos embedding (He et al., 2021) through the given relative indices of each patch. For discrete positional embeddings, we perform pretraining in MAE, since the discrete position can **not** represent the relative positions of two views. Therefore, for each image, we randomly mask the given image with 75% masking ratio. Then, we use the remain part to reconstruct the masked part. For learnable positional embedding, we first calculate the relative positional index proposed in Eq. 4. Then, we use a two-layer MLP to map the tuple (h, w) to D_{model} dimension as the positional embedding. For discrete sin-cos, we also adopt the MAE pretraining and the model degenerates to MAE (He et al., 2021) (replace the RGB supervision with teacher embeddings). Table 6 shows the classification and detection results on ImageNet and COCO, where our CR2PQ significantly outperforms peer methods.

Convergence and training efficiency. To explore the convergence of the proposed CR2PQ, we conduct a group of experiments with different pretraining epochs. Fig. 4 shows the detection and segmentation results on the COCO dataset with different pretraining epochs using Cascade-RCNN and Mask-RCNN frameworks. We surprisingly find with Cascade-RCNN, our CR2PQ can achieve 47.2 mAP^{bb} and 41.1 mAP^{mk} score with only 40 epochs pretraining, which obtains **10.4** improvements on mAP^{bb} and **7.9** improvements mAP^{mk} scores on detection and segmentation tasks, respectively. Besides, we also find with local loss, PQCL converges slower than without using the local loss (when 40 epochs pretraining, PQCL (w/o local) gets better results than w/ local)). However, with 200 epochs pretraining, PQCL (w/ local) outperforms PQCL (w/o local) by 0.7 mAP^{bb} and 1.7 mAP^{mk} scores. We guess that’s because the patch-level loss could impede the model from learning global-discriminative information, which slows down the convergence rate. However, the patch-level loss also makes the model learn spatial-sensitive information, resulting in better performance on detection and segmentation under long epochs pretraining. In contrast, CR2PQ enjoys fast convergence, and it outperforms previous SOTA by a large range with only 40 epochs pretraining.

Table 6: **Ablation on different pretraining strategy.** We pre-train ViT-S/16 with 300 epochs and 2048 batch size on ImageNet-1K and fine-tune on other datasets.

Student	Positional embedding	Epoch	Acc	mAP ^{bb}
ViT-S/16	Continuous 2D RoPE	300	82.2	50.5
	Discrete RoPE		81.5	48.2 (-2.3)
	Continuous Sin-cos		81.9	47.8 (-2.7)
	Learnable		81.3	46.9 (-3.6)
	Discrete Sin-cos		81.1	45.9 (-4.6)

5 CONCLUSION

In this paper, we propose CR2PQ to learn dense representations through continuous relative rotary positional embedding. Different from prior 2D RoPE works, we extend the discrete RoPE to continuous and demonstrate its effectiveness in learning dense representations from comprehensive experiments. Then, we conduct exhaustive ablation studies to demonstrate the robustness of the proposed CR2PQ, where our method achieves new SOTA results on detection and segmentation tasks, outperforming previous dense contrastive learning SOTA with a large range. Besides, our CR2PQ also achieves comparable results on classification with previous methods. Finally, we demonstrate the effectiveness of the proposed continuous RoPE through different positional embedding types.

Limitations. While CR2PQ achieves state-of-the-art results, there are limitations to consider for future exploration: Sensitivity to Background-heavy Views: The current method relies on randomly cropped views for contrastive learning (or distillation). In some cases, these views might contain mostly background with little foreground content. This can lead the model to learn irrelevant information that hinders performance on various downstream tasks focused on the foreground objects.

Broader Impact. The success of CR2PQ in transforming discrete RoPE to a continuous form and applying it to dense representation learning has the potential to significantly impact the field of computer vision. By demonstrating the effectiveness of continuous RoPE in dense tasks, this work could encourage the exploration and application of RoPE in various computer vision domains beyond those studied here. This could lead to advancements in tasks like image classification, object detection, and semantic segmentation, and further improve the robustness of vision models.

REFERENCES

- Adrien Bardes, Jean Ponce, and Yann LeCun. Vicreg: Variance-invariance-covariance regularization for self-supervised learning. In *ICLR*, 2022.
- Zhaowei Cai and Nuno Vasconcelos. Cascade r-cnn: Delving into high quality object detection. In *CVPR*, 2018.
- Mathilde Caron, Ishan Misra, Julien Mairal, Priya Goyal, Piotr Bojanowski, and Armand Joulin. Unsupervised learning of visual features by contrasting cluster assignments. *NeurIPS*, 2020.
- Mathilde Caron, Hugo Touvron, Ishan Misra, Hervé Jégou, Julien Mairal, Piotr Bojanowski, and Armand Joulin. Emerging properties in self-supervised vision transformers. In *ICCV*, 2021.
- Kai Chen, Jiaqi Wang, Jiangmiao Pang, Yuhang Cao, Yu Xiong, Xiaoxiao Li, Shuyang Sun, Wansen Feng, Ziwei Liu, Jiarui Xu, Zheng Zhang, Dazhi Cheng, Chenchen Zhu, Tianheng Cheng, Qijie Zhao, Buyu Li, Xin Lu, Rui Zhu, Yue Wu, Jifeng Dai, Jingdong Wang, Jianping Shi, Wanli Ouyang, Chen Change Loy, and Dahua Lin. MMDetection: Open mmlab detection toolbox and benchmark. *arXiv preprint arXiv:1906.07155*, 2019.
- Ting Chen, Simon Kornblith, Mohammad Norouzi, and Geoffrey Hinton. A simple framework for contrastive learning of visual representations. In *ICML*, 2020a.
- Xiaokang Chen, Mingyu Ding, Xiaodi Wang, Ying Xin, Shentong Mo, Yunhao Wang, Shumin Han, Ping Luo, Gang Zeng, and Jingdong Wang. Context autoencoder for self-supervised representation learning. *arXiv preprint arXiv:2202.03026*, 2022.
- Xinlei Chen and Kaiming He. Exploring simple siamese representation learning. In *CVPR*, 2021.
- Xinlei Chen, Haoqi Fan, Ross Girshick, and Kaiming He. Improved baselines with momentum contrastive learning. *arXiv preprint arXiv:2003.04297*, 2020b.
- Xinlei Chen, Saining Xie, and Kaiming He. An empirical study of training self-supervised vision transformers. In *ICCV*, 2021.
- MMSegmentation Contributors. MMSegmentation: Openmmlab semantic segmentation toolbox and benchmark. <https://github.com/open-mmlab/mmdetection>, 2020.
- Jia Deng, Wei Dong, Richard Socher, Li-Jia Li, Kai Li, and Li Fei-Fei. Imagenet: A large-scale hierarchical image database. In *CVPR*, 2009.
- Jeff Donahue and Karen Simonyan. Large scale adversarial representation learning. *NeurIPS*, 2019.
- Alexey Dosovitskiy, Lucas Beyer, Alexander Kolesnikov, Dirk Weissenborn, Xiaohua Zhai, Thomas Unterthiner, Mostafa Dehghani, Matthias Minderer, Georg Heigold, Sylvain Gelly, et al. An image is worth 16x16 words: Transformers for image recognition at scale. In *ICLR*, 2020.
- Yuxin Fang, Li Dong, Hangbo Bao, Xinggang Wang, and Furu Wei. Corrupted image modeling for self-supervised visual pre-training. *arXiv preprint arXiv:2202.03382*, 2022.
- Yuxin Fang, Quan Sun, Xinggang Wang, Tiejun Huang, Xinlong Wang, and Yue Cao. Eva-02: A visual representation for neon genesis. *arXiv preprint arXiv:2303.11331*, 2023.
- Chongjian Ge, Youwei Liang, Yibing Song, Jianbo Jiao, Jue Wang, and Ping Luo. Revitalizing cnn attention via transformers in self-supervised visual representation learning. *NeurIPS*, 2021.
- Spyros Gidaris, Praveer Singh, and Nikos Komodakis. Unsupervised representation learning by predicting image rotations. *arXiv preprint arXiv:1803.07728*, 2018.
- Ian Goodfellow, Jean Pouget-Abadie, Mehdi Mirza, Bing Xu, David Warde-Farley, Sherjil Ozair, Aaron Courville, and Yoshua Bengio. Generative adversarial nets. *NeurIPS*, 27, 2014.
- Jean-Bastien Grill, Florian Strub, Florent Altché, Corentin Tallec, Pierre Richemond, Elena Buchatskaya, Carl Doersch, Bernardo Avila Pires, Zhaohan Guo, Mohammad Gheshlaghi Azar, et al. Bootstrap your own latent-a new approach to self-supervised learning. *NeurIPS*, 2020.

594 Tengda Han, Weidi Xie, and Andrew Zisserman. Self-supervised co-training for video representation
595 learning. *NeurIPS*, 2020.

596

597 Kaiming He, Xiangyu Zhang, Shaoqing Ren, and Jian Sun. Deep residual learning for image
598 recognition. In *CVPR*, 2016.

599

600 Kaiming He, Georgia Gkioxari, Piotr Dollár, and Ross Girshick. Mask r-cnn. In *ICCV*, 2017.

601

602 Kaiming He, Haoqi Fan, Yuxin Wu, Saining Xie, and Ross Girshick. Momentum contrast for
603 unsupervised visual representation learning. In *CVPR*, 2020.

604

605 Kaiming He, Xinlei Chen, Saining Xie, Yanghao Li, Piotr Dollár, and Ross Girshick. Masked
606 autoencoders are scalable vision learners. *arXiv preprint arXiv:2111.06377*, 2021.

607

608 Pranav Jeevan and Amit Sethi. Resource-efficient hybrid x-formers for vision. In *WACV*, 2022.

609

610 Borui Jiang, Ruixuan Luo, Jiayuan Mao, Tete Xiao, and Yuning Jiang. Acquisition of localization
611 confidence for accurate object detection. In *ECCV*, 2018.

612

613 Yanghao Li, Hanzi Mao, Ross Girshick, and Kaiming He. Exploring plain vision transformer
614 backbones for object detection. In *ECCV*, 2022.

615

616 Tsung-Yi Lin, Michael Maire, Serge Belongie, James Hays, Pietro Perona, Deva Ramanan, Piotr
617 Dollár, and C Lawrence Zitnick. Microsoft coco: Common objects in context. In *ECCV*, 2014.

618

619 Tsung-Yi Lin, Piotr Dollár, Ross Girshick, Kaiming He, Bharath Hariharan, and Serge Belongie.
620 Feature pyramid networks for object detection. In *CVPR*, 2017.

621

622 Ilya Loshchilov and Frank Hutter. Sgdr: Stochastic gradient descent with warm restarts. *arXiv
623 preprint arXiv:1608.03983*, 2016.

624

625 Ilya Loshchilov and Frank Hutter. Fixing weight decay regularization in adam. 2018.

626

627 Jiasen Lu, Christopher Clark, Sangho Lee, Zichen Zhang, Savya Khosla, Ryan Marten, Derek Hoiem,
628 and Aniruddha Kembhavi. Unified-io 2: Scaling autoregressive multimodal models with vision,
629 language, audio, and action. *arXiv preprint arXiv:2312.17172*, 2023.

630

631 Aaron van den Oord, Yazhe Li, and Oriol Vinyals. Representation learning with contrastive predictive
632 coding. 2018.

633

634 Utku Ozbulak, Hyun Jung Lee, Beril Boga, Esra Timothy Anzaku, Ho-min Park, Arnout Van Messem,
635 Wesley De Neve, and Joris Vankerschaver. Know your self-supervised learning: A survey on
636 image-based generative and discriminative training. *TMLR*, 2023.

637

638 Jiaming Song and Stefano Ermon. Multi-label contrastive predictive coding. *NeurIPS*, 2020.

639

640 Jianlin Su, Murtadha Ahmed, Yu Lu, Shengfeng Pan, Wen Bo, and Yunfeng Liu. Roformer: Enhanced
641 transformer with rotary position embedding. *Neurocomputing*, 2024.

642

643 Chenxin Tao, Xizhou Zhu, Weijie Su, Gao Huang, Bin Li, Jie Zhou, Yu Qiao, Xiaogang Wang, and
644 Jifeng Dai. Siamese image modeling for self-supervised vision representation learning, 2022.

645

646 Yonglong Tian, Dilip Krishnan, and Phillip Isola. Contrastive multiview coding. In *ECCV*, 2020a.

647

Yonglong Tian, Chen Sun, Ben Poole, Dilip Krishnan, Cordelia Schmid, and Phillip Isola. What
makes for good views for contrastive learning? *NeurIPS*, 2020b.

Hugo Touvron, Matthieu Cord, Matthijs Douze, Francisco Massa, Alexandre Sablayrolles, and Hervé
Jégou. Training data-efficient image transformers & distillation through attention. In *ICML*, 2021.

Ashish Vaswani, Noam Shazeer, Niki Parmar, Jakob Uszkoreit, Llion Jones, Aidan N Gomez, Łukasz
Kaiser, and Illia Polosukhin. Attention is all you need. *NeurIPS*, 2017.

Pascal Vincent, Hugo Larochelle, Yoshua Bengio, and Pierre-Antoine Manzagol. Extracting and
composing robust features with denoising autoencoders. In *ICML*, 2008.

-
- Xiao Wang, Haoqi Fan, Yuandong Tian, Daisuke Kihara, and Xinlei Chen. On the importance of asymmetry for siamese representation learning. In *CVPR*, 2022a.
- Xinlong Wang, Rufeng Zhang, Chunhua Shen, Tao Kong, and Lei Li. Dense contrastive learning for self-supervised visual pre-training. In *CVPR*, 2021.
- Zhaoqing Wang, Qiang Li, Guoxin Zhang, Pengfei Wan, Wen Zheng, Nannan Wang, Mingming Gong, and Tongliang Liu. Exploring set similarity for dense self-supervised representation learning. In *CVPR*, 2022b.
- Chen Wei, Haoqi Fan, Saining Xie, Chao-Yuan Wu, Alan Yuille, and Christoph Feichtenhofer. Masked feature prediction for self-supervised visual pre-training. *arXiv preprint arXiv:2112.09133*, 2021.
- Tete Xiao, Yingcheng Liu, Bolei Zhou, Yuning Jiang, and Jian Sun. Unified perceptual parsing for scene understanding. In *ECCV*, 2018.
- Tete Xiao, Colorado J Reed, Xiaolong Wang, Kurt Keutzer, and Trevor Darrell. Region similarity representation learning. In *ICCV*, 2021.
- Enze Xie, Jian Ding, Wenhai Wang, Xiaohang Zhan, Hang Xu, Peize Sun, Zhenguo Li, and Ping Luo. Detco: Unsupervised contrastive learning for object detection. In *ICCV*, 2021a.
- Zhenda Xie, Yutong Lin, Zhuliang Yao, Zheng Zhang, Qi Dai, Yue Cao, and Han Hu. Self-supervised learning with swin transformers. *arXiv preprint arXiv:2105.04553*, 2021b.
- Zhenda Xie, Yutong Lin, Zheng Zhang, Yue Cao, Stephen Lin, and Han Hu. Propagate yourself: Exploring pixel-level consistency for unsupervised visual representation learning. In *CVPR*, 2021c.
- Zhenda Xie, Zheng Zhang, Yue Cao, Yutong Lin, Jianmin Bao, Zhuliang Yao, Qi Dai, and Han Hu. Simmim: A simple framework for masked image modeling. *CVPR*, 2022.
- Ceyuan Yang, Zhirong Wu, Bolei Zhou, and Stephen Lin. Instance localization for self-supervised detection pretraining. In *CVPR*, 2021.
- Sukmin Yun, Hankook Lee, Jaehyung Kim, and Jinwoo Shin. Patch-level representation learning for self-supervised vision transformers. In *CVPR*, 2022.
- Jure Zbontar, Li Jing, Ishan Misra, Yann LeCun, and Stéphane Deny. Barlow twins: Self-supervised learning via redundancy reduction. In *ICML*, 2021.
- Richard Zhang, Phillip Isola, and Alexei A Efros. Colorful image colorization. In *ECCV*, 2016.
- Shaofeng Zhang, Feng Zhu, Junchi Yan, Rui Zhao, and Xiaokang Yang. Zero-cl: Instance and feature decorrelation for negative-free symmetric contrastive learning. In *ICLR*, 2021.
- Shaofeng Zhang, Lyn Qiu, Feng Zhu, Junchi Yan, Hengrui Zhang, Rui Zhao, Hongyang Li, and Xiaokang Yang. Align representations with base: A new approach to self-supervised learning. In *CVPR*, 2022.
- Shaofeng Zhang, Qiang Zhou, Zhibin Wang, Fan Wang, and Junchi Yan. Patch-level contrastive learning via positional query for visual pretraining. In *ICML*, 2023a.
- Shaofeng Zhang, Feng Zhu, Rui Zhao, and Junchi Yan. Patch-level contrasting without patch correspondence for accurate and dense contrastive representation learning. In *ICLR*, 2023b.
- Bolei Zhou, Hang Zhao, Xavier Puig, Sanja Fidler, Adela Barriuso, and Antonio Torralba. Scene parsing through ade20k dataset. In *CVPR*, 2017.
- Jinghao Zhou, Chen Wei, Huiyu Wang, Wei Shen, Cihang Xie, Alan Yuille, and Tao Kong. Image BERT pre-training with online tokenizer. In *ICLR*, 2022.
- Adrian Ziegler and Yuki M Asano. Self-supervised learning of object parts for semantic segmentation. In *CVPR*, 2022.

A IMPLEMENTATION AND EXPERIMENT SETUPS

Baselines. We consider recent advanced self-supervised methods based on the ResNets (He et al., 2016) and ViTs (Dosovitskiy et al., 2020) architectures: (a) self-supervised ResNets: SimCLR (Chen et al., 2020a), MoCo-v2 (Chen et al., 2020b), SwAV (Caron et al., 2020), Barlow Twins (Zbontar et al., 2021), ZeroCL (Zhang et al., 2021), ARB (Zhang et al., 2022), DenseCL (Wang et al., 2021), ReSim (Xiao et al., 2021), and DetCo (Xie et al., 2021a); and (b) self-supervised ViTs: DINO (Caron et al., 2021), MoCo-v3 (Chen et al., 2021), MoBY (Xie et al., 2021b), iBOT (Zhou et al., 2022), SelfPatch (Yun et al., 2022), TinyMIM (Ozbulak et al., 2023).

Code of computing relative coordinates. Code 1 shows the implementation of how to compute relative coordinates matrix of \mathbf{rp}_B .

```

1 def factorial(p_A, p_B, K_A, K_B):
2     # p_A and p_B are given in line 199 of this paper.
3     # K_A, K_B are given in Eq.3 in this paper.
4     # width
5     w_per_grid_A = p_A[3] / K_A
6     w_grid_bias = (p_B[1] - p_A[1]) / w_per_grid_A
7     w_per_grid_B = p_B[3] / K_B
8     w_grid_scale = w_per_grid_B / w_per_grid_A
9     # height
10    h_per_grid_A = p_A[2] / K_A
11    h_grid_bias = (p_B[0] - p_A[0]) / h_per_grid_A
12    h_per_grid_B = p_B[2] / K_B
13    h_grid_scale = h_per_grid_B / h_per_grid_A
14    # compute coordinate matrix
15    h_start, h_end = h_grid_bias + K_B * h_grid_scale
16    w_start, w_end = w_grid_bias + K_B * w_grid_scale
17    grid_h = torch.arange(start=h_start, end=h_end, step=
18        h_grid_scale)
19    grid_w = torch.arange(start=w_start, end=w_end, step=
20        w_grid_scale)
21    grid = torch.meshgrid(grid_w, grid_h)
22    return grid

```

Listing 1: Computing Relative Coordinates

B EXPERIMENT ON LARGE-SCALE MODEL

To explore the scalability of the proposed CR2PQ, we conduct experiments with ViT-L, and evaluate the pretrained ViT-Base on ViTDet Li et al. (2022) detector. Specifically, we pre-train the ViT-Large with 800 epochs with batch size 2048, distributed on 16 A100 GPUs with the base learning rate $1.5e-4$. Table B shows the results on ImageNet-1K using ViT-L backbone, where our CR2PQ can consistently outperform previous baselines on both 400 and 800 epochs pretraining. Table B shows the results of the COCO dataset when using ViT-B as the backbone and ViTDet as the detector head.

Method	Architecture	Epoch	Acc@1
DINO (Caron et al., 2021)	ResNet-50	400	77.4
Moco V3 (Chen et al., 2021)	ViT-L/16	600	84.1
MAE (He et al., 2021)	ViT-L/16	400	84.3
CR2PQ (Teacher ResNet-50 DINO)	ViT-L/16	400	84.6
MAE (He et al., 2021)	ViT-L/16	800	84.6
iBOT (Zhou et al., 2022)	ViT-L/16	1000	84.8
CR2PQ (Teacher ResNet-50 DINO)	ViT-L/16	800	85.3

Table 7: Finetuning classification results on ImageNet-1K dataset using ViT-L.

Method	mAP ^{bb}	mAP ^{mk}
Scratch	48.1	42.6
MAE (He et al., 2021)	51.1	45.6
DINO (Caron et al., 2021)	49.0	43.4
CR2PQ (Ours)	52.2	46.5

Table 8: Object detection and instance segmentation results on COCO datasets using ViT-Base and ViTDet.